Photoacoustics xxx (2016) xxx–xxx

Contents lists available at ScienceDirect

Photoacoustics

journal homepage: www.elsevier.com/locate/pacs

Research article

Multimodal optoacoustic and multiphoton microscopy of human carotid atheroma

Markus Seeger[a,b,1], Angelos Karlas[a,b,c,1], Dominik Soliman[a,b], Jaroslav Pelisek[d], Vasilis Ntziachristos[a,b,*]

[a] Chair for Biological Imaging, Technische Universität München, Munich, Germany
[b] Institute of Biological and Medical Imaging, Helmholtz Zentrum München, Neuherberg, Germany
[c] Department of Cardiology, Klinikum rechts der Isar, Technische Universität München, Munich, Germany
[d] Department of Vascular and Endovascular Surgery, Klinikum rechts der Isar, Technische Universität München, Munich, Germany

ARTICLE INFO

Article history:
Received 14 March 2016
Received in revised form 14 May 2016
Accepted 25 July 2016

Keywords:
Human carotid atheroma
Collagen
Red blood cells
Multimodal microscopy
Optoacoustic microscopy
Photoacoustic microscopy
Non-linear optical microscopy

ABSTRACT

Carotid artery atherosclerosis is a main cause of stroke. Understanding atherosclerosis biology is critical in the development of targeted prevention and treatment strategies. Consequently, there is demand for advanced tools investigating atheroma pathology. We consider hybrid optoacoustic and multiphoton microscopy for the integrated and complementary interrogation of plaque tissue constituents and their mutual interactions. Herein, we visualize human carotid plaque using a hybrid multimodal imaging system that combines optical resolution optoacoustic (photoacoustic) microscopy, second and third harmonic generation microscopy, and two-photon excitation fluorescence microscopy. Our data suggest more comprehensive insights in the pathophysiology of atheroma formation and destabilization, by enabling congruent visualization of structural and biological features critical for the atherosclerotic process and its acute complications, such as red blood cells and collagen.

1. Introduction

Atherosclerosis, a multifactorial disease of the arterial wall, is a major precursor of ischemic heart disease and stroke; two of the leading morality causes worldwide [1]. Ischemic stroke is attributed to thrombosis and cerebral ischemia and often associated with chronic atheromatous plaque accumulating within the sub-endothelial layer (intima) of carotid arteries. Effective plaque prevention or treatment requires understanding of the mechanisms underlying atheroma formation, rupture, and consequent precipitation to acute ischemic events.

Atheroma tissue obtained from patients is a highly valuable source of information regarding the disease. It typically presents an inhomogeneous mass of high structural and biological complexity, usually consisting of lipids, inflammatory and smooth muscle cells (SMC), connective tissue, and calcium deposits [2–4]. Multiple factors (e.g. inflammatory, biomechanical, genetic, environmental) seem to be involved in all stages of atheroma formation and progression [3,4].

The discrete histopathological features of atherosclerotic plaques, reflecting different pathogenetic and pathophysiological mechanisms, allow for classification according to their severity: early, intermediate, and advanced [5]. Early lesions usually start as simple clusters of lipid-loaded macrophages before reforming to so-called fatty streaks and giving rise to discrete lipid pools among the SMC layers along with discrete intimal thickening [6]. Intermediate lesions are the first to be described as atheromas, since they have a well-defined core of lipids usually protruding into the vascular lumen. In terms of clinical incidence, early lesions are asymptomatic while intermediate ones may already cause

Abbreviations: BF, Brightfield; CAE, Carotid thrombendarterectomy; CMR, Continuous multirecord; DAQ, Data acquisition; FOV, Field of view; GM, Galvanometric mirrors; HE, Hemalaun-Eosin; IPH, Intraplaque hemorrhage; LDL, Low density lipoprotein; MAP, Maximum amplitude projection; MPM, Multiphoton microscopy; MPOM, Multiphoton and optoacoustic microscopy; NLO, Non-linear optical; OAM, Optoacoustic microscopy; PMT, Photo multiplier tube; PSR, Picro-Sirius Red; RBC, Red blood cell; ROI, Region of interest; SHG, Second harmonic generation; SMC, Smooth muscle cell; THG, Third harmonic generation; TPEF, Two-photon excitation fluorescence.

* Corresponding author at: Chair for Biological Imaging, Technische Universität München, Munich, Germany and Institute of Biological and Medical Imaging, Helmholtz Zentrum München, Neuherberg, Germany.
E-mail addresses: markus.seeger@tum.de (M. Seeger), v.ntziachristos@tum.de (V. Ntziachristos).
[1] Equal contribution.

http://dx.doi.org/10.1016/j.pacs.2016.07.001

ischemic disturbances [7,8]. However, the presence of symptoms is usually connected to advanced (late) and complicated plaques even if the phenomenon of plaque rupture seems to be uncorrelated to parameters such as plaque size and degree of luminal narrowing [7,9]. Advanced lesions are characterized by a thinning of the fibrous cap and a large lipid core containing an increased amount of collagen, inflammatory cells, as well as affected SMCs. These plaques may evolve into complicated ones with superficial fissure formation, intraplaque hemorrhage (IPH), and acute luminal thrombus occurrence due to direct exposure of lipid core material to blood contents [4,5,8].

From a topographical point of view, each plaque may be roughly divided into sections corresponding to specific structural regions: the cap, the shoulders, and the core (Fig. 2a). According to multiple histological studies, thrombosis is usually the result of cap ulceration and rupture near to one of the shoulders [10–12]. A vulnerable plaque is generally characterized by a large necrotic core (lipids, fibrin, blood inclusions, and macrophages), a thin degraded cap (decreased collagen and SMCs), as well as prominent inflammatory and neovascularization features [13]. Plaque rupture is frequently considered to be a mechanical event. On the one hand, collagen, a basic constituent of the extracellular matrix, seems to be associated with the biomechanical integrity of the cap [14]. Its degradation and disorganization have been correlated to decreased stability of the fibrous cap [14,15], while the retrieval of collagen production (e.g. statin therapy) seems to stabilize the plaque [16]. On the other hand, red blood cells (RBC), either within the plaque's neovessels or in the form of IPH, play a crucial role in atheroma progression, destabilization, and rupture [13].

With respect to the above mentioned histopathological evolution of atheromatous lesions linked to topographical conditions and compositions at specific regions within the plaque, new powerful and accurate imaging tools are required to precisely observe and analyse components influencing the mechanical stability. Within this framework, the accurate identification and characterization of the histological components of an atheromatous sample could increase our knowledge about atherosclerosis and define features related to ischemic events, which would potentially serve as future therapeutic targets.

Studies of atheromas largely rely on histopathology [17–21], which can interrogate several cellular and molecular features of the disease. Conversely, histopathology is invasive and laborious, requires tissue staining, and typically visualizes thin slices and small areas of the specimen. Non-invasive volumetric or quantitative measurements of excised atheromas are studied by tissue-sectioning microscopy, such as confocal or multiphoton microscopy [22–25]. Nevertheless, tissue-sectioning microscopy also requires labels for cellular and sub-cellular moieties. While genetically modified animals using fluorescent reporter labels may be generated for studying atheroma events in mice, imaging of excised human specimens is problematic for use with tissue-sectioning microscopy since it requires diffusion and clearance of a label through the tissue post-mortem. Likewise, the use of fluorescence agents against specific atheroma targets have been used in animal studies [26–29], but are not readily available for human use.

The use of non-linear optical (NLO) microscopy has been suggested for label-free visualization of atheromas, based on optical harmonic detection or tissue autofluoresence. It has been shown that second harmonic generation (SHG) microscopy resolves collagen structures, two-photon excitation fluorescence (TPEF) microscopy probes nicotinamide adenine dinucleotide

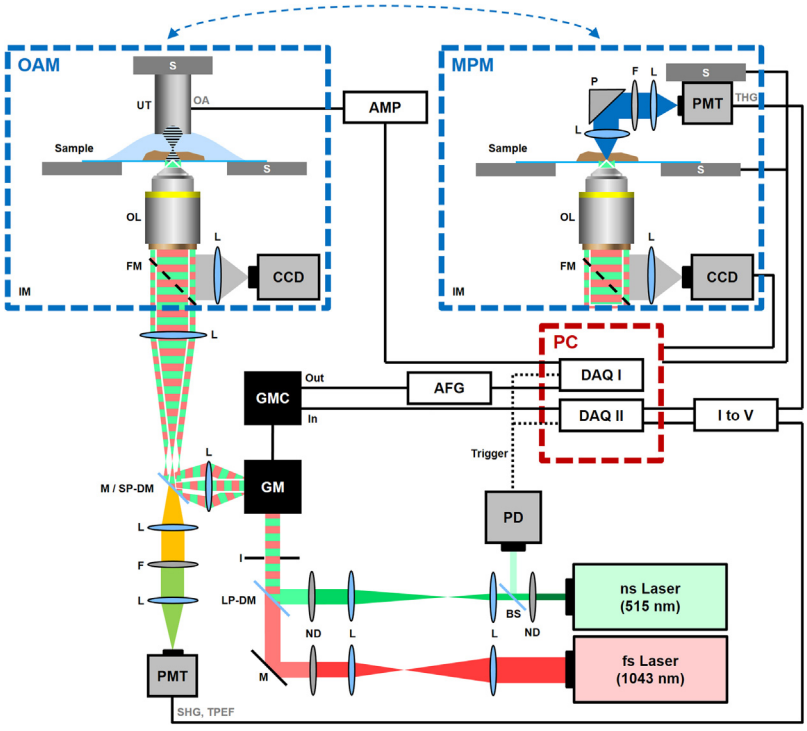

Fig. 1. Schematic depiction of the MPOM system consisting of two interchangeable microscopy systems, namely OAM and MPM. Abbreviations: AFG, arbitrary function generator; AMP, amplifier; BS, beamsplitter; DAQ, data acquisition card; F, optical filter; FM, flippable mirror; GM, galvanometric mirrors; GMC, GM control; I, iris diaphragm; L, lens; LP-DM, longpass dichroic mirror; M, mirror; ND, neutral density filter; OA, optoacoustic signal; OL, microscope objective lens; P, prism; PD, photodiode; PMT, photomultiplier tube; S, xyz stage; SHG, second harmonic generation signal; SP-DM, shortpass dichroic mirror; UT, ultrasound transducer; THG, third harmonic generation signal; TPEF, two-photon excitation fluorescence signal.

Please cite this article in press as: M. Seeger, et al., Multimodal optoacoustic and multiphoton microscopy of human carotid atheroma, Photoacoustics (2016), http://dx.doi.org/10.1016/j.pacs.2016.07.001

(NADH), elastin, and foam cells, whereby third harmonic generation (THG) microscopy can image low density lipoprotein (LDL) deposits or embedded macrophages [30–35]. Optoacoustic imaging has also been investigated for imaging atheroma and vascular moieties regarding the detection as well as distinction of lipids and hematomas [36–39]. Recently, multiphoton and optoacoustic microscopy were proposed for hybrid imaging of autofluorescence, harmonic, and absorption contrast generation [40–42], so far applied to visualize structural and cellular features in fish and small mammals.

Herein we consider the extension of label-free imaging capacities by applying multiphoton microscopy (MPM) and optoacoustic microscopy (OAM) in a pilot study to characterize atheromatous tissue. We studied whether the hybrid approach could reveal a wider feature set of investigational or clinical relevance without the need to stain or label the tissue. Using the intrinsically accurate registration of optical and optoacoustic microscopy images, we further researched the spatial congruence and complementarity of collagen and RBCs in human carotid atheroma, i.e. two basic components which are present in different stages of the plaque formation process and frequently altered in unstable plaques [17].

2. Materials and methods

2.1. Experimental setup

The hybrid microscopic system utilized in this study combines second and third harmonic generation (SHG and THG), two-photon excitation fluorescence (TPEF), and optical resolution optoacoustic microscopy (OAM). All modalities are characterized by a lateral resolution of about 1 μm and an imaging depth of up to ~300 μm [40,41]. Hybrid multiphoton and optoacoustic microscopy (MPOM), as schematically depicted in Fig. 1, consists of two separate laser systems for OAM and MPM [40,41]. Both laser systems are based on a common and co-aligned beam path, which is guided consecutively into an inverted microscope (AxioObserver. D1, Zeiss, Jena, Germany). Final image generation for both systems is achieved by raster-scanning a focused optical excitation beam across the examined specimen by means of fast galvanometric mirrors (GM) (6215H, Cambridge Technology, Bedford, USA). An accurate and seamless interchange between ultrasound transducer for OAM and photomultiplier tube (PMT) for THG acquisition is accomplished by magnetic kinematic bases (SB1/M & SB1T/M, Thorlabs, New Jersey, USA), which are previously adjusted using a suture-cross reference phantom (Dafilon USP 11/0, B. Braun Melsungen AG, Melsungen, Germany). Brightfield (BF) examination of chosen regions of interest (ROI) was carried out using a CCD camera (AxioCam ICc 1, Zeiss).

2.2. Optoacoustic microscopy (OAM)

OAM utilizes a pulsed diode-pumped solid-state laser (Flare HP PQ Green 2k 500, Innolight GmbH, Hannover, Germany; energy per pulse: 570 μJ, pulse width: 1.8 ns, repetition rate: 1.2 kHz) as an excitation source at 515 nm. The beam is attenuated by neutral density filters and enlarged by a telescopic arrangement of lenses. In order to merge both modalities, the OAM beam is guided by a longpass dichroic mirror (DMLP650, Thorlabs) onto a high-precision set of GMs. Latter are used for raster-scanning the beam focus in the sample and are controlled by a 16 bit data acquisition card (DAQ) (PCIe 6363, National Instruments, Austin, Texas, USA; max. sampling rate per channel: 1 MS/s). Subsequently, the beam is focused by a microscope objective lens (Plan Apochromat 10X, Zeiss, Jena, Germany; air immersion, NA: 0.45) to a diffraction limited spot through a 170 μm thick glass slide on top of which the sample is placed (see 2.5 *Sample preparation*). For OAM detection, a spherically focused 100 MHz transducer (SONAXIS, Besancon, France; bandwidth: ~10–180 MHz, focal distance: 2.85 mm, active element diameter: 3 mm) is located in transmission mode with respect to the illumination above the sample. Acoustic coupling is provided by a water droplet between sample and transducer. The acquired optoacoustic signals are amplified by 63 dB (AU 1291, Miteq, New York, USA) and recorded by a high-speed 12 bit DAQ card (ADQ412, SP Devices, Linköping, Sweden; max. sampling rate per channel: 3.6 GS/s). Adjustment of the setup and alignment of both the optical and the acoustic foci co-axially to one another is achieved by two high-precision motorized xyz-stages (MLS203-2 & MZS500, Thorlabs; M-683.2U4 & M-501.1DG, Physik Instrumente GmbH & Co. KG, Karlsruhe, Germany), as described in more detail in [41]. In order to cover the scanned region of the optical beam with the acoustic sensitive field, the transducer is placed 700 μm in positive defocus with respect to the optical focal plane.

Both DAQ cards, and thus the acquisition as well as the movement of the GMs, are triggered by a photodiode (DET36A, Thorlabs) and thereby synchronized to the laser repetition rate. In order to generate an OAM image, a field of view (FOV) of 630 μm × 630 μm with a resolution of 600 × 600 pixels and a pixel averaging of 20 is recorded by step wise raster-scanning the beam across the sample. To assign the OAM signals with the corresponding position or rather pixel in the final image, the direct current (DC) coupled position feedback of the GMs is amplitude modulated by an alternating current (AC) generated by an arbitrary waveform function generator (DG1022, Rigol Technologies Inc., Beaverton, USA) to be recordable by the AC coupled high-speed DAQ card. Both the amplified time-resolved optoacoustic signals as well as the actual positions are acquired at 450 MS/s by means of a continuous multirecord (CMR) mode, a streaming-like acquisition mode in which records stored in temporary buffers on the internal memory of the DAQ card are fetched to the computer memory while acquiring the remaining records. In OAM, raw signals are bandpass filtered in the range of 10–180 MHz and their maximum amplitude is extracted to generate an unprocessed maximum amplitude projection (MAP) image. The synchronization of both DAQ cards, control of the raster-scan by means of GMs, the CMR based data acquisition, as well as filtering and projection of raw OAM signals is fully performed in Matlab (Matlab 2014a, Mathworks, Natick, USA).

2.3. Multiphoton microscopy (MPM)

The MPM subsystem of MPOM, as comprehensively described in [40,41], employs a Yb-based solid-state laser (YBIX, Time-Bandwidth, Zurich, Switzerland; energy per pulse: 30 nJ, pulse width: 170 fs, repetition rate: 84.4 MHz) to excite the specimen at 1043 nm in order to generate NLO effects, namely SHG, THG, and TPEF. Whereas the THG signal is acquired in transmission mode, SHG and TPEF signals are acquired in backward direction after filtering out the laser excitation with a shortpass dichroic mirror (DMSP805R, Thorlabs). The NLO signals are separated using optical filters (SHG (FB520-10), THG (FGUV11), TPEF (FELH0550), Thorlabs) and are recorded by highly sensitive PMTs (H9305 03, Hamamatsu, Hamamatsu City, Japan). Digitizing is achieved by the previously mentioned 16 bit DAQ card, which is also controlling the GM scanning with a predefined scanning frequency of 320 kHz. MPM images in this work are acquired in a FOV of 630 μm × 630 μm with a resolution of 800 × 800 pixels and an image averaging of 100. For the purpose of optimizing the superposition of all MPOM modalities, direction and collimation of both beams prior to entering the microscope objective lens are achieved by a shearing interferometer (SI050, Thorlabs). Chromatic deviation in z between the foci of the two laser systems are corrected by the

Please cite this article in press as: M. Seeger, et al., Multimodal optoacoustic and multiphoton microscopy of human carotid atheroma, Photoacoustics (2016), http://dx.doi.org/10.1016/j.pacs.2016.07.001

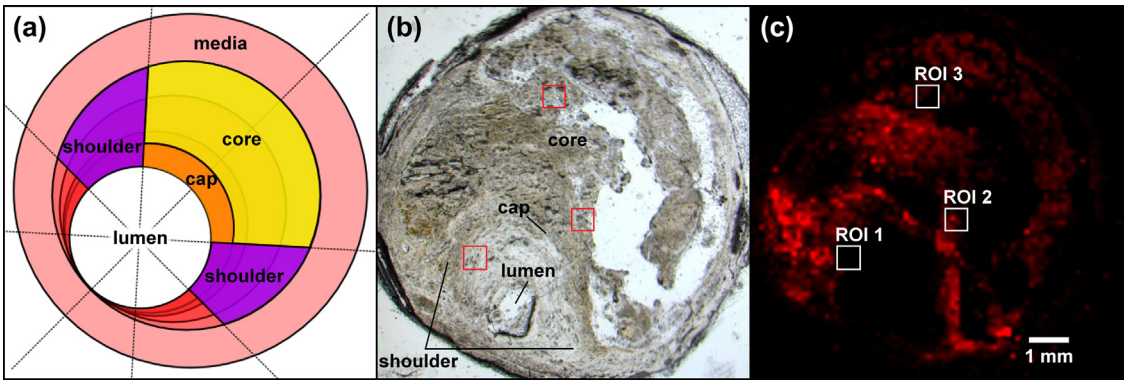

Fig. 2. Coarse imaging and ROI selection of human carotid atheroma. (a) Schematic depiction of a typical atherosclerotic vascular cross-section. (b) Widefield BF observation of the unstained atheroma sample used for MPOM imaging and identification of lumen, cap, and shoulders. (c) Coarse OAM scan indicating a progressed intraplaque RBC embedding. Final ROI selection for subsequent MPOM imaging is indicated by the red and white boxes.

sample holding xyz-stage. MPM image acquisition as well as controlling of both xyz-stages is carried out by LabVIEW programs [40,41].

2.4. Imaging protocol and image registration

Widefield BF images (Aperio CS2, Leica, Wetzlar, Germany) could be complemented by acquiring coarse optoacoustic imaging over a 10 mm × 10 mm FOV performing a mechanical scan of the sample holding xyz-stage with a large step size of 100 μm. Then, specific ROIs could be selected on the large FOV images for high-resolution visualization by OAM and MPM. Prior to MPM examination, the water droplet used as acoustic coupling medium between transducer and sample for OAM imaging was removed. Image processing and co-registration of the four modalities were carried out in ImageJ (ImageJ 1.50e, Wayne Rasband). OAM and MPM images were upsampled by bicubic interpolation, median filtered, and histogram-wise adjusted to saturate 1% of the pixels. Final co-registration of all modalities was performed by using the built-in function StackReg executing an affine transformation whereas the TPEF image was used as an "anchor" for the OAM images [43]. Through exciting the sample at two close wavelengths (TPEF: 521.5 nm; OAM: 515 nm), the corresponding obtained signals lead to partially shared information content although the

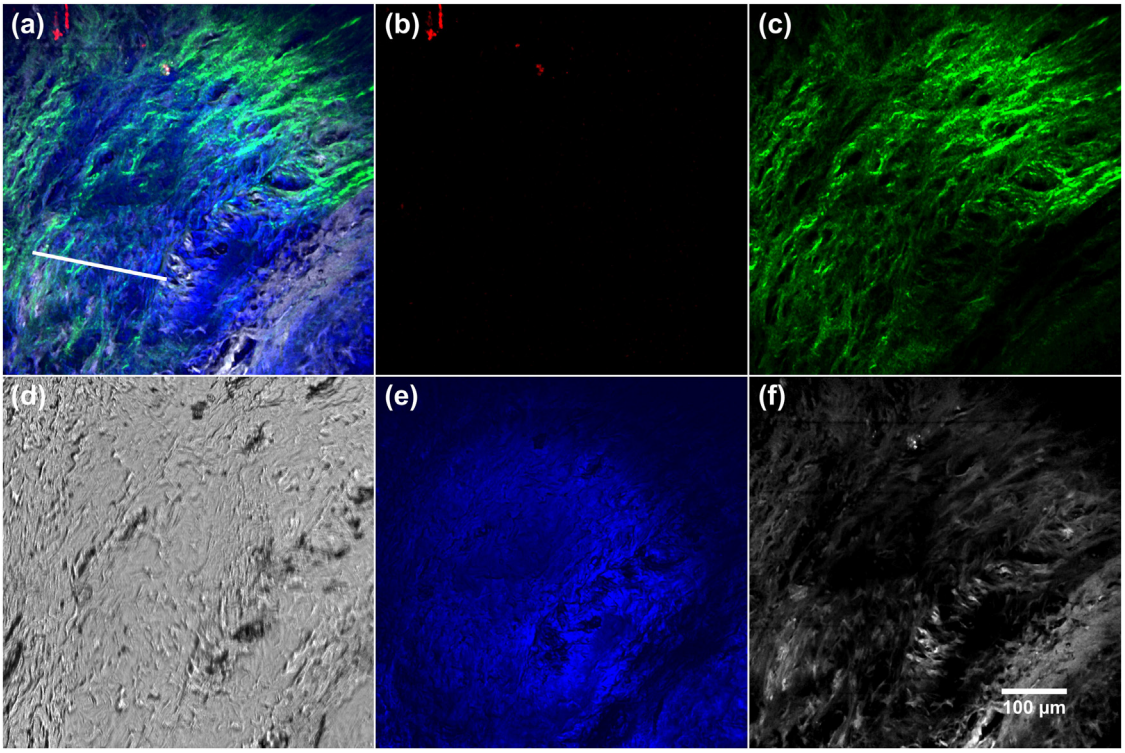

Fig. 3. Hybrid microscopy imaging of human carotid atheroma at the shoulder region (ROI 1). (a) Overlay of OA, SHG, THG, and TPEF demonstrates an unscathed condition of the connective tissue (e.g. collagen and elastin), no large inclusions or fissures, and a negligible amount of embedded blood residues. Separate depiction of (b) RBC embeddings (OAM), (c) collagen (SHG), (d) tissue appearance (BF), (e) tissue morphology (THG), and (f) mainly elastin (TPEF). Profile for subsequent analysis is indicated by the white line in (a).

Please cite this article in press as: M. Seeger, et al., Multimodal optoacoustic and multiphoton microscopy of human carotid atheroma, Photoacoustics (2016), http://dx.doi.org/10.1016/j.pacs.2016.07.001

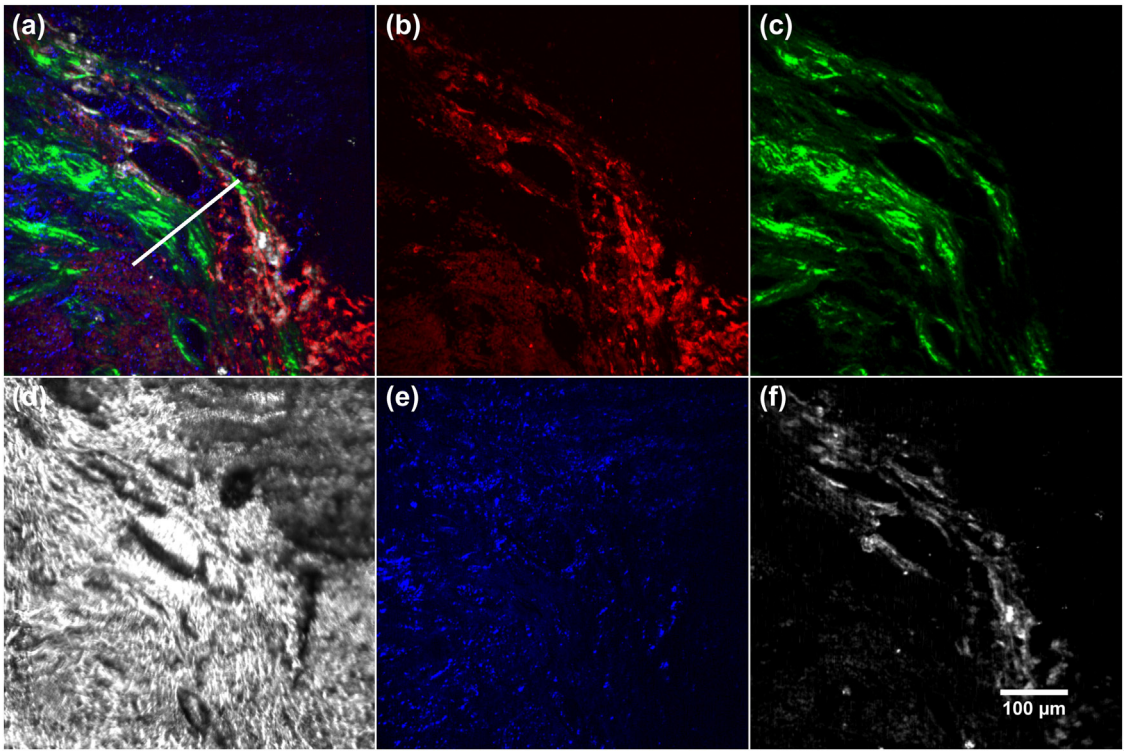

Fig. 4. Hybrid microscopy imaging of human carotid atheroma at the cap region (ROI 2). (a) Overlay of OAM, SHG, THG, and TPEF indicates coarse interleaving structure of embedded blood residues and connective tissue bands of collagen and elastin. Separate depiction of (b) RBC embeddings (OAM), (c) collagen (SHG), (d) tissue appearance (BF), (e) tissue morphology (THG), and (f) mainly elastin and RBCs (TPEF). Profile for subsequent analysis is indicated by the white line in (a).

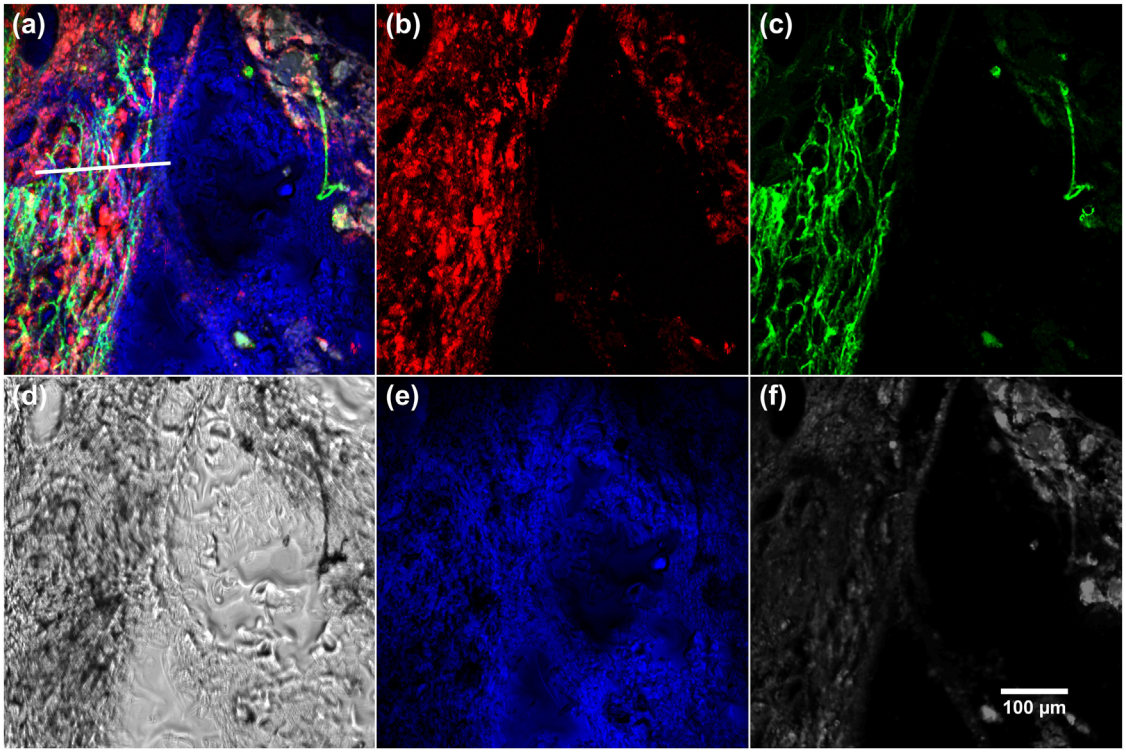

Fig. 5. Hybrid microscopy imaging of human carotid atheroma at the lipid core (ROI 3). (a) Overlay of OAM, SHG, THG, and TPEF reveals fine interleaving structure of embedded blood residues and collagen bands. Separate depiction of (b) RBC embeddings (OAM), (c) collagen (SHG), (d) tissue appearance (BF), (e) tissue morphology (THG), and (f) elastin, LDL, foam cells, and RBCs (TPEF). Profile for subsequent analysis is indicated by the white line in (a).

Please cite this article in press as: M. Seeger, et al., Multimodal optoacoustic and multiphoton microscopy of human carotid atheroma, Photoacoustics (2016), http://dx.doi.org/10.1016/j.pacs.2016.07.001

signal generation differs. OAM relies on an absorption contrast, such as the one from hemoglobin stored in RBCs, whereas TPEF detects natural fluorochromes such as elastin. Nevertheless, we found that these two signatures could be accurately registered.

2.5. Sample preparation

A human atherosclerotic tissue sample was acquired from a patient with advanced carotid artery stenosis, who underwent carotid thrombendarterectomy (CAE). The surgically removed atherosclerotic plaque was further segmented in blocks of 3–4 mm length, fixed in formalin overnight, and subsequently embedded in paraffin. Each segment was further cut into 10 μm thick slices and the selected samples were placed on thin glass slides (170 μm) to facilitate hybrid MPOM imaging. In order to assess the plaque morphology, three different staining procedures were applied: Hemalaun-Eosin (HE) to evaluate plaque cellularity, Picro-Sirius Red (PSR) to visualize collagen fibres, and Orcein to show elastin fibres. Herein, three different slices were chosen, which were directly adjacent to the unstained slice used for hybrid MPOM imaging within the same sample. For the validation of our methods and to demonstrate its capabilities, we present standard histological images of the approximate same positions in the sample (Aperio CS2, Leica) [44,45].

3. Results

First, we examined the appearance of widefield BF and coarse OAM images with respect to topological features of atherosclerotic tissue samples. Fig. 2a depicts a schematic subdivision of atheromas, which is sectioned into structural regions such as the lumen, the shoulders, the cap, and the core. Fig. 2b presents a widefield BF image of the sample. Fig. 2c shows a co-registered coarse OAM scan of the whole sample, obtained in the same orientation as in Fig. 2b. Fig. 2 preliminary reveals a complementarity between color contrast seen on Fig. 2b and absorption contrast seen on Fig. 2c. In particular, a characteristic intraplaque yellow-brown pattern throughout the tissue sample, possibly due to embedded RBC residues, is also visualized as an optoacoustic signal pattern in Fig. 2c.

The coarse examination of Fig. 2 allows for the overall assessment of the sample regarding its global morphology, narrowing of the lumen, level of degradation, and, thus, the estimation of the degree of severity and the potential risk of rupture. Based on these coarse sample images we could then select specific plaque compartments for studying their fine local topological structure using the MPOM modalities. We selected ROIs close to the lumen in the shoulder region (ROI 1), centred at the cap (ROI 2), and in the lipid core (ROI 3).

Fig. 3 depicts the MPOM examination of ROI 1 close to the former lumen in the shoulder region. Fig. 3a presents a composite image combining OAM, SHG, THG, and TPEF images. Fig. 3b shows the RBC distribution imaged by OAM, Fig. 3c shows the collagen structure imaged by SHG, Fig. 3d is the BF appearance of ROI 1, Fig. 3e is the THG image representative of the overall cell morphology, and Fig. 3f shows the elastin network yielded by TPEF. The merged image (Fig. 3a) demonstrates no clear mutual interaction among the imaged components and reveals an intact connective tissue. No prominent RBC clusters are present. Moreover, collagen and elastin appear largely fibrillar, ribbon shaped, and unfractured. Regarding the cell morphology, no inclusions or fissures larger than a few tens of micrometres can be seen.

Fig. 4 shows MPOM images from ROI 2. As previously, the merged image is shown in Fig. 4a and the OAM, SHG, BF, THG, and TPEF images are shown in Fig. 4b–f, respectively. Fig. 4a represents the merged image and exhibits marked differences compared to Fig. 3a. A pattern of embedded RBCs, resolved by OAM, appears co-localized with the connective tissue, i.e. collagen revealed by SHG and elastin revealed by TPEF. Furthermore, a coarse alternating structure of RBC inclusions and connective tissue can be seen. In ROI 2 THG and BF observation reveal a slightly disturbed cell morphology including fissures and inclusions in the range of 10–100 μm.

Fig. 5 illustrates MPOM images of the lipid core (ROI 3), in the same order followed for Figs. 3 and 4. As obvious in the merged overlay (Fig. 5a), there is congruence between blood residues (OAM) and collagen fibres (SHG) in the lipid core. Embedded RBCs appear in clusters, whereby collagen fibres appear widened and split up into smaller fibrils. A fine interleaving of these two structure can be seen. Furthermore, TPEF reveals the presence of round-shaped structures in the upper right corner, which cannot be assigned with OAM signals generally indicating blood residues.

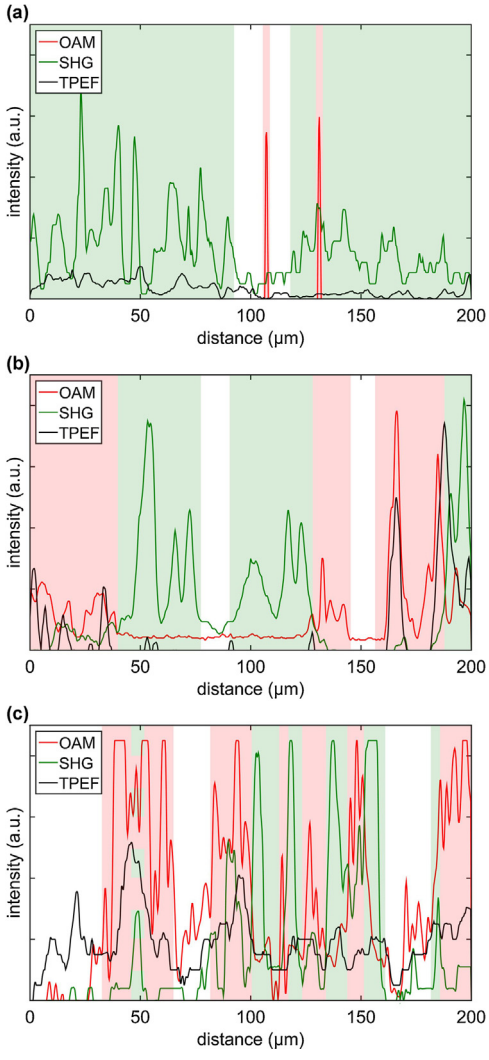

Fig. 6. Profiles of embedded blood residues, collagen, and elastin along the white lines indicated in Figs. 3 –5 a. The interleaving interaction between intraplaque coagulated RBCs and collagen occurs on different size levels leading to undisturbed collagen bands (a; ROI 1), coarse interrupted collagen stripes (b; ROI 2), and fine expanded structures (c; ROI 3). Partially shared signatures among OAM and TPEF reveal blood distribution whereas signals occurring only in TPEF present elastin within the sample. Colored areas represent the dominant compound in the respective region (red: RBC (OAM); green: collagen (SHG)).

Please cite this article in press as: M. Seeger, et al., Multimodal optoacoustic and multiphoton microscopy of human carotid atheroma, Photoacoustics (2016), http://dx.doi.org/10.1016/j.pacs.2016.07.001

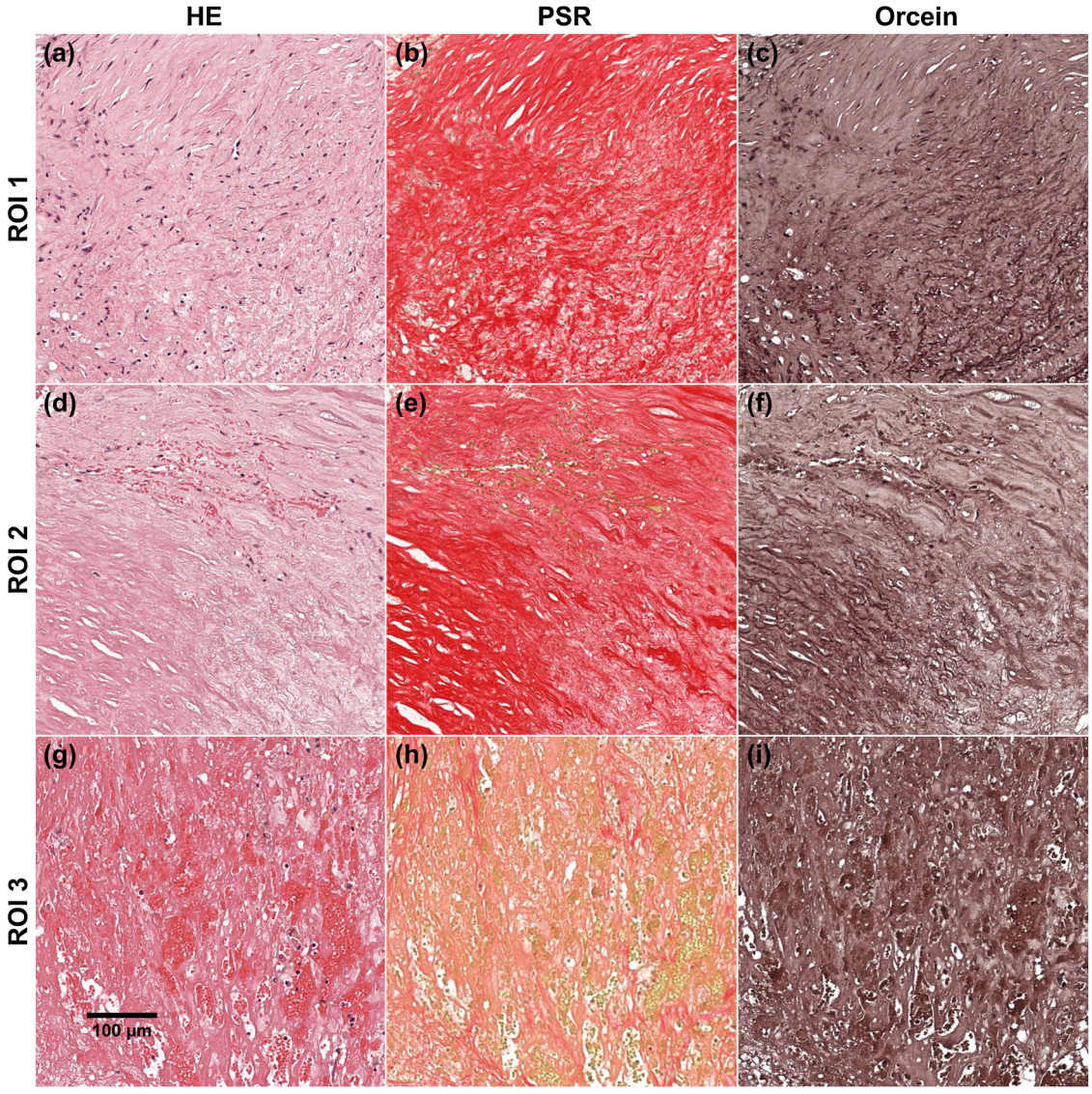

Fig. 7. Histological images of human carotid atheroma validating MPOM performance. (a) HE staining of cell nuclei (blue), cytoplasm (pink), and RBCs (dark red), (b) PSR staining of collagen (dark red), and (c) Orcein staining of elastin of the sample regions at the shoulder (ROI 1). Analogous depiction of (d,g) HE, (e,h) PSR, and (f,i) Orcein stainings for ROI 2 and ROI 3, respectively.

Thus, this pattern might indicate inclusions of LDL and foam cells, which are prominent in the lipid core. Finally, an advanced degradation of cell morphology can be observed.

Fig. 6 plots the OAM, SHG, and TPEF profiles along the white lines marked in Figs. 3 a, 4 a, and 5 a, and allows for the observation of the spatial scale of the corresponding structures. The plots demonstrate different interleaved patterns of SHG and OAM signals at different scales depending on the observed ROI. Fig. 6a, obtained close to the lumen (ROI 1), confirms the lack of congruence between RBCs and collagen. The SHG profile indicates an intact collagen ribbon of at least 200 μm width consisting of individual collagen strands of 2–10 μm diameter. In contrast, Fig. 6b visualizes a coarse widening of the collagen bands (ROI 2). Large gaps in the range of 80–100 μm indicate partially intact collagen ribbons interleaved with areas of embedded RBCs. Fig. 6c plots the most advanced interaction between RBCs and collagen recorded from the three ROIs. These interleaving structures, observed in the lipid core (ROI 3), occur in the range of 8–15 μm. Although the widths of detected collagen fibrils match the ones seen in ROI 1 (Fig. 6a), assumed as an unharmed collagen structure, these strands are separated from one another by incorporated RBCs.

In a next step we compared the MPOM findings with conventional histopathology images, acquired from approximately the same regions imaged by MPOM (Fig. 7). HE staining of cell nuclei, cytoplasm, and RBCs, PSR staining of collagen, and Orcein staining of elastin are depicted in the first, second, and third column of Fig. 7, respectively, for three specimens obtained from the shoulder (ROI 1), the cap (ROI 2), and the lipid core (ROI 3) region. Whereas at the shoulder region only single RBCs are present (Fig. 7a), the cap region is characterized by larger RBC inclusions (Fig. 7d), and the lipid core contains widely spread RBC coagulated aggregates (Fig. 7g). In addition, the collagen as well as the elastin structures tend to widen and expand from an unharmed and strong regular shape at the shoulder region (Fig. 7b and c), through an intermediate situation at the cap (Fig. 7e and f), to a fine subdivided distribution in the lipid core (Fig. 7h and i). It can be also observed that single fibrillar structures, such as collagen and elastin, cannot be unambiguously identified. These observations

Please cite this article in press as: M. Seeger, et al., Multimodal optoacoustic and multiphoton microscopy of human carotid atheroma, Photoacoustics (2016), http://dx.doi.org/10.1016/j.pacs.2016.07.001

confirm differences in histological appearance between the three examined ROIs and complement the MPOM findings.

4. Discussion

We investigated label-free visualization of human atheroma using multimodal optical and optoacoustic microscopy. Label-free imaging is researched herein as a complementary method to conventional histopathology analysis. An increasing number of label-free contrast mechanisms can thus visualize histopathologically interesting compounds such as erythrocytes, collagen, elastin, foam cells, macrophages, and the overall tissue morphology by the combination of OAM and NLO microscopy methods [40,41]. Even though OAM was implemented herein at a single wavelength, imaging at multiple wavelengths can further increase the number of labels available to the multimodal system, e.g. enabling the visualization of lipids.

The hybrid microscopy aimed at revealing different structural and morphological components of human atheroma and demonstrated the ability to co-localize readings of RBCs, elastin, collagen, lipid, and other moieties. Type I and II collagen can be imaged using SHG due to the collagen's non-centrosymmetry and birefringence properties [46–49]. Based on intrinsic autofluoresence, elastin, LDL, foam cells, and to a smaller extent embedded RBCs can be probed by TPEF [46–48], whereas THG is sensitive to the overall tissue morphology due to optical interface heterogeneities such as cell boundaries [47,50]. Finally, embedded RBCs are visualized by OAM based on the strong optical absorption of hemoglobin in the visible range in combination with a low quantum yield [51,52].

In the healthy arterial wall, which shows a viscoelastic behaviour, collagen (along with elastin) represents the elastic component and warrants vessel stability, while arterial wall viscosity is mainly reflected by the function of SMCs. According to basic studies, in the load-free wall (*ex vivo*), the collagen fibres seem to be corrugated. On the other side, under strong wall stresses, collagen fibrils are being elongated, reaching their elastic limit and offering enhanced mechanical strength to the arterial wall [53]. Regarding atheromatous tissue, collagen synthesis and degradation influences plaque stability and progression: Excessive collagen production may accelerate stenosis, while collagen decomposition seems to be correlated with increased rupture susceptibility [54]. Furthermore, RBCs are thought to be a potential contributor to atheroma accumulation and progression [55]. Both neovascularization and IPH are considered as basic factors of increased plaque vulnerability [56]. From a histological point of view, the profile of a vulnerable plaque shows the following features: 1) a large lipid core, 2) a small number of SMCs, low quantity and quality of collagen within the fibrous cap, 3) enhanced accumulation of inflammatory cells (macrophages and T-lymphocytes) in the shoulder regions and the cap, and 4) the presence of neovessels and IPH [21]. According to this data, the intraplaque statuses of collagen and RBCs are critical elements of plaque vulnerability.

In the current study, we presented data visualizing collagen, elastin, and RBC congruence within a human carotid sample. MPOM reveals these moieties without the need of staining. Therefore, composite signals can be acquired from the same slice without the need to interleave and stain slices, leading to a precise topological co-registration between different signals. Further optimization of the current system could allow for the simultaneous detection of other constituents (e.g. lipids), giving a wider possibility for stain-free investigation of tissues. In the future, detailed microscopic observations of atheroma could be combined with macroscopical observations for example employing multispectral optoacoustic tomography (MSOT) [57].

Conflict of interest statement

The authors declare that there are no conflicts of interest.

Authors contribution

M.S. performed, processed, and analysed the imaging experiments. A.K. guided the experiments and their interpretation medically. D.S. helped in conducting the experiments. J.P. provided the human atheromatous plaque sample and carried out the histological staining and examination. V.N. conceptualised the idea of the hybrid microscope and supervised all steps of this project. M. S., A.K., and V.N. wrote the manuscript whereas all authors contributed to the improvement and completion of the article.

Acknowledgments

The authors acknowledge funding from the DFG as part of the CRC 1123 (Z1) and the DFG Reinhard Koselleck project (NT 3/9-1).

References

[1] WHO, 2014, WHO, The top 10 causes of death, Fact Sheet N°310 (Updated May 2014) (2014) http://www.who.int/mediacentre/factsheets/fs310/en/.
[2] W. Insull, The pathology of atherosclerosis: plaque development and plaque responses to medical treatment, Am. J. Med. 122 (2009) S3–S14, doi:http://dx.doi.org/10.1016/j.amjmed.2008.10.013.
[3] B.C. Dickson, A.I. Gotlieb, Towards understanding acute destabilization of vulnerable atherosclerotic plaques, Cardiovasc. Pathol. 12 (2003) 237–248, doi:http://dx.doi.org/10.1016/S1054-8807(03)00072-3.
[4] R.B. Singh, S.A. Mengi, Y.J. Xu, A.S. Arneja, N.S. Dhalla, Pathogenesis of atherosclerosis: a multifactorial process, Exp. Clin. Cardiol. 7 (2002) 40–53.
[5] R. Virmani, A. Burke, E. Ladich, F.D. Kolodgie, Pathology of carotid artery atherosclerotic disease, Carotid Dis., 1st ed., Cambridge Univ. Press, Cambridge, United Kingdom, 2007, pp. 1–2, doi:http://dx.doi.org/10.1017/CBO9780511544941.002.
[6] H.C. Stary, A.B. Chandler, S. Glagov, J.R. Guyton, W. Insull Jr., M.E. Rosenfeld, et al., A definition of initial, fatty streak, and intermediate lesions of atherosclerosis. A report from the Committee on Vascular Lesions of the Council on Arteriosclerosis, American Heart Association, Circulation 89 (1994) 2462–2478, doi:http://dx.doi.org/10.1161/01.cir.89.5.2462.
[7] D.E. Gutstein, V. Fuster, Pathophysiology and clinical significance of atherosclerotic plaque rupture, Cardiovasc. Res. 41 (1999) 323–333, doi:http://dx.doi.org/10.1016/S0008-6363(98)00322-8.
[8] H.C. Stary, A.B. Chandler, R.E. Dinsmore, V. Fuster, S. Glagov, W. Insull, et al., A definition of advanced types of atherosclerotic lesions and a histological classification of atherosclerosis: a report from the Committee on Vascular Lesions of the Council on Arteriosclerosis, American Heart Association, Circulation 92 (1995) 1355–1374, doi:http://dx.doi.org/10.1161/01.CIR.92.5.1355.
[9] J.M. Mann, M.J. Davies, Vulnerable plaque. Relation of characteristics to degree of stenosis in human coronary arteries, Circulation 94 (1996) 928–931, doi:http://dx.doi.org/10.1161/01.CIR.94.5.928.
[10] E. Falk, P.K. Shah, V. Fuster, Coronary plaque disruption, Circulation 92 (1995) 657–671, doi:http://dx.doi.org/10.1161/01.CIR.92.3.657.
[11] P.D. Richardson, M.J. Davies, G.V.R. Born, Influence of plaque configuration and stress distribution on fissuring of coronary atherosclerotic plaques, Lancet 334 (1989) 941–944, doi:http://dx.doi.org/10.1016/S0140-6736(89)90953-7.
[12] G. Pasterkamp, A.H. Schoneveld, A.C. van der Wal, D.J. Hijnen, W.J. van Wolveren, S. Plomp, et al., Inflammation of the atherosclerotic cap and shoulder of the plaque is a common and locally observed feature in unruptured plaques of femoral and coronary arteries, Arterioscler. Thromb. Vasc. Biol. 19 (1999) 54–58, doi:http://dx.doi.org/10.1161/01.ATV.19.1.54.
[13] D.A. Chistiakov, A.N. Orekhov, Y.V. Bobryshev, Contribution of neovascularization and intraplaque haemorrhage to atherosclerotic plaque progression and instability, Acta Physiol. 213 (2015) 539–553, doi:http://dx.doi.org/10.1111/apha.12438.
[14] S.K. Nadkarni, B.E. Bouma, J. De Boer, G.J. Tearney, Evaluation of collagen in atherosclerotic plaques: the use of two coherent laser-based imaging methods, Lasers Med. Sci. 24 (2009) 439–445, doi:http://dx.doi.org/10.1007/s10103-007-0535-x.
[15] J.O. Deguchi, E. Aikawa, P. Libby, J.R. Vachon, M. Inada, S.M. Krane, et al., Matrix metalloproteinase-13/collagenase-3 deletion promotes collagen accumulation and organization in mouse atherosclerotic plaques, Circulation 112 (2005) 2708–2715, doi:http://dx.doi.org/10.1161/CIRCULATIONAHA.105.562041.
[16] P. Libby, M. Aikawa, Mechanisms of plaque stabilization with statins, Am. J. Cardiol. 91 (2003) 4B–8B, doi:http://dx.doi.org/10.1016/S0002-9149(02)03267-8.

[17] K.-R. Purushothaman, M. Purushothaman, P. Muntner, P.A. Lento, W.N. O'Connor, S.K. Sharma, et al., Inflammation, neovascularization and intraplaque hemorrhage are associated with increased reparative collagen content: implication for plaque progression in diabetic atherosclerosis, Vasc. Med. 16 (2011) 103–108, doi:http://dx.doi.org/10.1177/1358863X11402249.
[18] J.F. Bentzon, F. Otsuka, R. Virmani, E. Falk, Mechanisms of plaque formation and rupture, Circ. Res. 114 (2014) 1852–1866, doi:http://dx.doi.org/10.1161/CIRCRESAHA.114.302721.
[19] R. Virmani, Atherosclerotic plaque progression and vulnerability to rupture: angiogenesis as a source of intraplaque hemorrhage, Arterioscler. Thromb. Vasc. Biol. 25 (2005) 2054–2061, doi:http://dx.doi.org/10.1161/01.ATV.0000178991.71605.18.
[20] J. Milei, J.C. Parodi, M. Ferreira, A. Barrone, D.R. Grana, L. Matturri, Atherosclerotic plaque rupture and intraplaque hemorrhage do not correlate with symptoms in carotid artery stenosis, J. Vasc. Surg. 38 (2003) 1241–1247, doi:http://dx.doi.org/10.1016/S0741-5214(03)00910-8.
[21] R. Virmani, F.D. Kolodgie, A.P. Burke, A. Farb, S.M. Schwartz, Lessons from sudden coronary death, Arterioscler. Thromb. (2000) 1262–1275, doi:http://dx.doi.org/10.1161/01.ATV.20.5.1262.
[22] M. Van Zandvoort, W. Engels, K. Douma, L. Beckers, M. Oude Egbrink, M. Daemen, et al., Two-photon microscopy for imaging of the (Atherosclerotic) vascular wall: a proof of concept study, J. Vasc. Res. 41 (2004) 54–63, doi:http://dx.doi.org/10.1159/000076246.
[23] S. Massberg, K. Brand, S. Gruner, S. Page, E. Muller, I. Muller, et al., A critical role of platelet adhesion in the initiation of atherosclerotic lesion formation, J. Exp. Med. 196 (2002) 887–896, doi:http://dx.doi.org/10.1084/jem.20012044.
[24] S. Massberg, M. Gawaz, S. Gruner, V. Schulte, I. Konrad, D. Zohlnhofer, et al., A crucial role of glycoprotein VI for platelet recruitment to the injured arterial wall in vivo, J. Exp. Med. 197 (2002) 41–49, doi:http://dx.doi.org/10.1084/jem.20020945.
[25] W. Yu, J.C. Braz, A.M. Dutton, P. Prusakov, M. Rekhter, In vivo imaging of atherosclerotic plaques in apolipoprotein E deficient mice using nonlinear microscopy, J. Biomed. Opt. 12 (2007) 054008, doi:http://dx.doi.org/10.1117/1.2800337.
[26] H. Yoo, J.W. Kim, M. Shishkov, E. Namati, T. Morse, R. Shubochkin, et al., Intra-arterial catheter for simultaneous microstructural and molecular imaging in vivo, Nat. Med. 17 (2011) 1680–1684, doi:http://dx.doi.org/10.1038/nm.2555.
[27] F.A. Jaffer, M.A. Calfon, A. Rosenthal, G. Mallas, R.N. Razansky, A. Mauskapf, et al., Two-dimensional intravascular near-infrared fluorescence molecular imaging of inflammation in atherosclerosis and stent-induced vascular injury, J. Am. Coll. Cardiol. 57 (2011) 2516–2526, doi:http://dx.doi.org/10.1016/j.jacc.2011.02.036.
[28] M.A. Calfon, C. Vinegoni, V. Ntziachristos, F.A. Jaffer, Intravascular near-infrared fluorescence molecular imaging of atherosclerosis: toward coronary arterial visualization of biologically high-risk plaques, J. Biomed. Opt. 15 (2010) 011107, doi:http://dx.doi.org/10.1117/1.3280282.
[29] C. Vinegoni, I. Botnaru, E. Aikawa, M.A. Calfon, Y. Iwamoto, E.J. Folco, et al., Indocyanine green enables near-infrared fluorescence imaging of lipid-rich, Inflamed Atherosclerotic Plaques 3 (2011) 1–20, doi:http://dx.doi.org/10.1126/scitranslmed.3001577.Indocyanine.
[30] T.T. Le, I.M. Langohr, M.J. Locker, M. Sturek, J.-X. Cheng, Label-free molecular imaging of atherosclerotic lesions using multimodal nonlinear optical microscopy, Biomed. Microdevices 12 (2009) 1–20, doi:http://dx.doi.org/10.1117/1.2795437.Label-free.
[31] M.B. Lilledahl, O.A. Haugen, C. de Lange Davies, L.O. Svaasand, Characterization of vulnerable plaques by multiphoton microscopy, J. Biomed. Opt. 12 (2014) 044005, doi:http://dx.doi.org/10.1117/1.2772652.
[32] L.B. Mostaço-Guidolin, M.G. Sowa, A. Ridsdale, A.F. Pegoraro, M.S.D. Smith, M. D. Hewko, et al., Differentiating atherosclerotic plaque burden in arterial tissues using femtosecond CARS-based multimodal nonlinear optical imaging, Biomed. Opt. Express 1 (2010) 59–73, doi:http://dx.doi.org/10.1364/BOE.1.000059.
[33] F.A. Jaffer, M.A. Calfon, A. Rosenthal, G. Mallas, R.N. Razansky, A. Mauskapf, et al., Two-dimensional intravascular near-infrared fluorescence molecular imaging of inflammation in atherosclerosis and stent-induced vascular injury, J. Am. Coll. Cardiol. 57 (2011) 2516–2526, doi:http://dx.doi.org/10.1016/j.jacc.2011.02.036.
[34] H.-W. Wang, T.T. Le, J.-X. Cheng, Label-free imaging of arterial cells and extracellular matrix using a multimodal CARS microscope, Opt. Commun. 281 (2008) 1813–1822, doi:http://dx.doi.org/10.1016/j.optcom.2007.07.067.
[35] H.-W. Wang, I.M. Langohr, M. Sturek, J.-X. Cheng, Imaging and quantitative analysis of atherosclerotic lesions by CARS-based multimodal nonlinear optical microscopy, Arterioscler. Thromb. Vasc. Biol. 29 (2009) 1342–1348, doi:http://dx.doi.org/10.1161/ATVBAHA.109.189316.
[36] K. Jansen, M. Wu, A.F.W. van der Steen, G. van Soest, Photoacoustic imaging of human coronary atherosclerosis in two spectral bands, Photoacoustics 2 (2014) 12–20, doi:http://dx.doi.org/10.1016/j.pacs.2013.11.003.
[37] A. Petrov, K.E. Wynne, M.A. Parsley, I.Y. Petrov, Y. Petrov, K.A. Ruppert, et al., Optoacoustic detection of intra- and extracranial hematomas in rats after blast injury, Photoacoustics 2 (2014) 75–80, doi:http://dx.doi.org/10.1016/j.pacs.2014.04.001.
[38] S. Sethuraman, J.H. Amirian, S.H. Litovsky, R.W. Smalling, S.Y. Emelianov, Spectroscopic intravascular photoacoustic imaging to differentiate atherosclerotic plaques, Opt. Express 16 (2008) 3362–3367, doi:http://dx.doi.org/10.1364/OE.16.003362.
[39] B. Wang, J.L. Su, J. Amirian, S.H. Litovsky, R. Smalling, S. Emelianov, Detection of lipid in atherosclerotic vessels using ultrasound-guided spectroscopic intravascular photoacoustic imaging, Opt. Express 18 (2010) 4889–4897, doi:http://dx.doi.org/10.1364/OE.18.004889.
[40] G.J. Tserevelakis, D. Soliman, M. Omar, V. Ntziachristos, Hybrid multiphoton and optoacoustic microscope, Opt. Lett. 39 (2014) 1819–1822, doi:http://dx.doi.org/10.1364/OL.39.001819.
[41] D. Soliman, G.J. Tserevelakis, M. Omar, V. Ntziachristos, Combining microscopy with mesoscopy using optical and optoacoustic label-free modes, Nat. Publ. Gr. (2015) 1–9, doi:http://dx.doi.org/10.1038/srep12902.
[42] B. Rao, F. Soto, D. Kerschensteiner, L.V. Wang, Integrated photoacoustic, confocal, and two-photon microscope, J. Biomed. Opt. 19 (2014) 36002, doi:http://dx.doi.org/10.1117/1.JBO.19.3.036002.
[43] P. Thévenaz, U.E. Ruttimann, M. Unser, A pyramid approach to subpixel registration based on intensity, IEEE Trans. Image Process. 7 (1998) 27–41, doi:http://dx.doi.org/10.1109/83.650848.
[44] J. Pelisek, J. Pongratz, L. Deutsch, C. Reeps, T. Stadlbauer, H.-H. Eckstein, Expression and cellular localization of metalloproteases ADAMs in high graded carotid artery lesions, Scand. J. Clin. Lab. Invest. (2012) 1–9, doi:http://dx.doi.org/10.3109/00365513.2012.734394.
[45] J. Pelisek, G. Well, C. Reeps, M. Rudelius, A. Kuehnl, M. Culmes, et al., Neovascularization and angiogenic factors in advanced human carotid artery stenosis, Circ. J. 76 (2012) 1274–1282, doi:http://dx.doi.org/10.1253/circj.CJ-11-0768.
[46] A. Zoumi, A. Yeh, B.J. Tromberg, Imaging cells and extracellular matrix in vivo by using second-harmonic generation and two-photon excited fluorescence, Proc. Natl. Acad. Sci. U. S. A. 99 (2002) 11014–11019, doi:http://dx.doi.org/10.1073/pnas.172368799.
[47] H. Segawa, M. Okuno, H. Kano, P. Leproux, V. Couderc, H. Hamaguchi, Label-free tetra-modal molecular imaging of living cells with CARS, SHG, THG and TSFG (coherent anti-stokes Raman scattering, second harmonic generation, third harmonic generation and third-order sum frequency generation), Opt. Express 20 (2012) 9551, doi:http://dx.doi.org/10.1364/oe.20.009551.
[48] J. Mansfield, J. Yu, D. Attenburrow, J. Moger, U. Tirlapur, J. Urban, et al., The elastin network: its relationship with collagen and cells in articular cartilage as visualized by multiphoton microscopy, J. Anat. 215 (2009) 682–691, doi:http://dx.doi.org/10.1111/j.1469-7580.2009.01149.x.
[49] X. Chen, O. Nadiarynkh, S. Plotnikov, P.J. Campagnola, Second harmonic generation microscopy for quantitative analysis of collagen fibrillar structure, Nat. Protoc. 7 (2012) 654–669, doi:http://dx.doi.org/10.1038/nprot.2012.009\rnprot.2012.009 pii.
[50] B. Weigelin, G.-J. Bakker, P. Friedl, Third harmonic generation microscopy of cells and tissue organization, J. Cell Sci. (2016) 245–255, doi:http://dx.doi.org/10.1242/jcs.152272.
[51] J. Yao, L.V. Wang, Sensitivity of photoacoustic microscopy, Photoacoustics 2 (2014) 87–101, doi:http://dx.doi.org/10.1016/j.pacs.2014.04.002.
[52] V. Ntziachristos, D. Razansky, Molecular imaging by means of multispectral optoacoustic tomography (MSOT), Chem. Rev. 110 (2010) 2783–2794, doi:http://dx.doi.org/10.1021/cr9002566.
[53] T.C. Gasser, R.W. Ogden, G.A. Holzapfel, Hyperelastic modelling of arterial layers with distributed collagen fibre orientations, J. R. Soc. Interface 3 (2006) 15–35, doi:http://dx.doi.org/10.1098/rsif.2005.0073.
[54] M.D. Rekhter, Collagen synthesis in atherosclerosis: too much and not enough, Cardiovasc. Res. 41 (1999) 376–384, doi:http://dx.doi.org/10.1016/S0008-6363(98)00321-6.
[55] G. Pasterkamp, R. Virmani, The erythrocyte: a new player in atheromatous core formation, Heart 88 (2002) 115–116, doi:http://dx.doi.org/10.1136/heart.88.2.115.
[56] A.V. Finn, R.K. Jain, Coronary plaque neovascularization and hemorrhage, JACC Cardiovasc. Imaging 3 (2010) 41–44, doi:http://dx.doi.org/10.1016/j.jcmg.2009.11.001.
[57] A. Dima, V. Ntziachristos, Non-invasive carotid imaging using optoacoustic tomography, Opt. Express 20 (2012) 25044, doi:http://dx.doi.org/10.1364/oe.20.025044.

Markus Seeger holds a M.Sc. degree in Biophysics awarded by the Institute of Biophysics (IfB) associated to the Goethe University of Frankfurt (JWGU), Frankfurt am Main, Germany. Within his master study he accomplished an international cooperation project at the Fudan University (FDU), Shanghai, China. He is currently working towards a Ph.D. degree at the Chair for Biological Imaging (CBI) at the Technical University of Munich (TUM) and at the Institute of Biological and Medical Imaging (IBMI) at the Helmholtz Zentrum Munich (HMGU), Munich, Germany. His research activities focus on the utilization of multimodal optoacoustic and optical techniques for microscopic and spectroscopic examination biological samples as well as the development of corresponding biomedical applications.

Please cite this article in press as: M. Seeger, et al., Multimodal optoacoustic and multiphoton microscopy of human carotid atheroma, Photoacoustics (2016), http://dx.doi.org/10.1016/j.pacs.2016.07.001

Angelos Karlas studied Medicine and Electrical and Computer Engineering at Aristotle University of Thessaloniki (AUTH), Greece. He holds a M.Sc. degree in Medical Informatics from the Aristotle University of Thessaloniki, as well as a M.Res. in Medical Robotics and Image Guided Intervention from the Imperial College London (ICL), London, UK. He currently works as a clinical resident at the Department of Cardiology, University Hospital Rechts der Isar (MRI), Munich, Germany, while pursuing his Dr. rer.nat. in Experimental Medicine at Technical University of Munich (TUM), Munich, Germany. His main research interests include advanced molecular imaging techniques with translational applications to the cardiovascular system.

Dominik Soliman studied Physics at the Technical University Munich (TUM) and completed his diploma on particle physics at the Excellence Cluster "Origin and Structure of the Universe", Garching, Germany. He is currently a Ph.D. student at the Chair for Biological Imaging (CBI) at the Technical University of Munich (TUM) and at the Institute of Biological and Medical Imaging (IBMI) at the Helmholtz Zentrum Munich (HMGU), Munich, Germany. His research interests include optoacoustic microscopy in time and frequency domain, the application of optoacoustic mesoscopy in biological imaging, as well as the development of hybrid optoacoustic and optical microscopy techniques.

Jaroslav Pelisek is an expert on the field of vascular biology. He has studied Molecular Biology and Genetics at the Ludwig-Maximilian-University (LMU), Munich, Germany, where he received his Dr.rer.nat from the Department of Cardiology and Angiology. He moved then to the Technical University of Munich (TUM), to the Department of Vascular and Endovascular Surgery at the University Hospital Rechts der Isar (MRI), Munich, Germany, where he attained postdoctoral lecture qualification. His research field concerns atherosclerosis of peripheral vessels and abdominal aortic aneurysm, epigenetics, and molecular biomarkers.

Vasilis Ntziachristos studied electrical engineering at Aristotle University in Thessaloniki (AUTH), Greece, and received his Master's and Doctorate degrees from the Bioengineering Department of the University of Pennsylvania (PENN), Philadelphia, USA. After completing a postdoc at the Center for Molecular Imaging Research (CMIR) at Harvard Medical School (HMS), he served as an instructor and then Assistant Professor and Director of the Laboratory for Bio-Optics and Molecular Imaging at Harvard University and Massachusetts General Hospital (MGH), Boston, USA. He is currently a Professor of Medicine, Professor of Electrical Engineering and Chair for Biological Imaging (CBI) at the Technical University of Munich (TUM) and the Director of the Institute of Biological and Medical Imaging (IBMI) at the Helmholtz Zentrum Munich (HMGU), Munich, Germany. His scientific focus lies on basic research and translation of novel optical and optoacoustic *in vivo* imaging technologies for addressing unmet biological and clinical needs.

Please cite this article in press as: M. Seeger, et al., Multimodal optoacoustic and multiphoton microscopy of human carotid atheroma, Photoacoustics (2016), http://dx.doi.org/10.1016/j.pacs.2016.07.001